J Solid State Electrochem (2012) 16:963–975
DOI 10.1007/s10008-011-1470-0

ORIGINAL PAPER

Electrochemical characterization of praseodymium centers in $Pr_xZr_{1-x}O_2$ zirconias using electrocatalysis and photoelectrocatalysis

Antonio Doménech · Noemí Montoya · Javier Alarcón

Received: 13 May 2011 / Revised: 7 June 2011 / Accepted: 8 June 2011 / Published online: 23 June 2011

Abstract The voltammetry of nanoparticles and scanning electrochemical microscopy are applied to characterize praseodymium centers in tetragonal and monoclinic zirconias, doped with praseodymium ions ($Pr_xZr_{1-x}O_2$), prepared via sol–gel routes. Doped zirconia nanoparticles were synthesized by a sol–gel liquid-phase route and characterized by different techniques, including X-ray diffraction powder pattern, ultraviolet–visible diffuse reflectance spectroscopy, infrared spectroscopy, and transmission electron microscopy (TEM). Gels annealed at around 400 °C yielded tetragonal $Pr_xZr_{1-x}O_2$ phases. The monoclinic forms of Pr-doped ZrO_2 were obtained by annealing at temperatures higher than 1,100 °C. TEM micrographs proved that the size of the nanoparticles produced was dependent on their crystalline form, around 15 and 60 nm for tetragonal and monoclinic, respectively. The electrochemical study confirmed that a relatively high content of praseodymium cation was in the chemical state (IV), i.e., as Pr^{4+}, in both zirconia host lattices. The catalytic and photocatalytic effects of Pr^{4+} centers located in the monoclinic zirconia lattice on nitrite reduction and oxygen evolution reaction were studied.

Keywords Praseodymium · Zirconia · Voltammetry of microparticles · Electrocatalysis · Photoelectrocatalysis

A. Doménech (✉)
Departament de Química Analítica, Universitat de València,
Dr. Moliner, 50,
46100 Burjassot, València, Spain
e-mail: antonio.domenech@uv.es

N. Montoya · J. Alarcón
Departament de Química Inorgànica, Universitat de València,
Dr. Moliner, 50,
46100 Burjassot, València, Spain

Introduction

Along the last decades, the preparation of rare earth (RE) doped oxide materials has received considerable attention. ZrO_2 materials doped with praseodymium ions ($Pr_xZr_{1-x}O_2$) have been extensively investigated as a consequence of their applications for oxygen storage [1], sensing [2–4], signal transport [5], catalysis [6], and thermal barrier coatings [7]. Such materials have been also tested for biomedical applications [8] and as potential cathodes for low-temperature solid oxide fuel cells [9].

Recently, some reports on $Pr_xZr_{1-x}O_2$ materials deal with the synthesis and X-ray powder diffraction (XRD) characterization of doped zirconia crystalline forms [10] and the spectral characteristics of monoclinic and tetragonal $Pr_xZr_{1-x}O_2$ [11–14]. Although it is frequently assumed that praseodymium acts as a typical trivalent rare earth element, it is possible to expect that this element can also exhibit a +4 oxidation state when stabilized in zirconia host. In fact, it is known that at low temperatures praesodymia, by itself, can form a wide range of ordered intermediate phases between PrO_2 and Pr_2O_3 [15], with a structural chemistry similar to that of ceria [16]. Thus, Pawlak et al. [14] have reported that Pr^{4+} can be stabilized in Pr plus Mg-codoped ytrium–aluminum–garnet, a widely used material for solid-state lasers, after annealing the material in a relatively oxidizing atmosphere (air) on the basis of the spectral characteristics of $(Y_{1-x-y}Pr_xMg_y)_3Al_5O_{12}$ ($x = 0.012$, $y = 5 \times 10^{-6}$) materials.

From the above reports, it seems possible that in both monoclinic and tetragonal zirconias the praseodymium cation can be present in several oxidation states. However, it can also be drawn that by using spectroscopic and magnetic techniques it is quite difficult to establish unambiguously the presence of these several oxidation

states of doping species and discern possible distinct coordinative environments. As far as such aspects are of interest for elucidating the properties of the resulting material, it appears to be pertinent the consideration of experimental techniques able to provide complementary information regarding these matters.

In previous reports, we have used the voltammetry of microparticles (VMP), a solid-state electrochemical technique developed by Scholz et al. [17–19], for obtaining chemical and structural information [20, 21] and analytical applications [22, 23] on zirconias doped with vanadium and cerium ions and zirconium minerals [24]. Here, we present a VMP study devoted to the characterization of the oxidation state and structural environment of praseodymium centers in nanoparticulate monoclinic and tetragonal Pr-doped zirconias. This study is focused on the elucidation of the oxidation state of praseodymium rather than on recording specific nanoparticle features. From the results obtained in the electrochemistry study of $Pr_xZr_{1-x}O_2$, it seemed interesting to check their possibilities to electrocatalyze the nitrite reduction in the aqueous medium in order to remark possible differences between doping centers, thus extending a previous analysis of chromium-doped cassiterite and tin-sphene ceramic materials [25].

Electrocatalytic reduction of nitrite is a problem of special interest from biochemical and environmental viewpoints [26]. In addition, the electrocatalytic reduction of nitrite ions in aqueous solution has received a great deal of interest in respect of developing sensitive and selective methods for its determination [27, 28]. Among others, the catalytic effect of transition metal oxides [29], metal complexes [30], redox-active films [31], and Keggin-type and Dawson-type polyoxometalate polymers [32–34] and model compounds for nitrite reductase immobilized into polymer films [35] have been studied. Photoelectrochemical reduction of nitrite was searched on the surface of an electrochemically roughened silver electrode [36] and semiconductor photocatalysts CdS [37]. The photoelectrochemical oxidation of nitrite has been studied at TiO_2/Ti materials [38, 39]. Complementary electrocatalytic experiments on the oxygen evolution reaction (OER) were also performed.

Here, solid specimens, which were prepared by sol–gel methods and characterized by different experimental techniques, were attached to paraffin-impregnated graphite electrodes in contact with sodium acetate/acetic acid aqueous electrolytes. Cyclic and square wave voltammetries were used as detection modes, being the later technique of particular interest because of its high sensitivity and immunity to capacitive effects [40]. Voltammetric techniques have been complemented with scanning electrochemical microscopy (SECM), a technique developed by Bard et al. [41] which provides information on electrochemical activity and surface topography at the nanoscopic level [42].

Experimental

Preparation of specimens $Pr_xZr_{1-x}O_2$

For the preparation of the nanoparticles, a sol–gel liquid-phase route was used because it is more versatile with regard to the controlled variation of structural, compositional, and morphological features of the final products, even though annealing is required to develop the nanoparticles in the desired crystalline form. Gels with compositions in the range $Pr_xZr_{1-x}O_2$, $0 \le x \le 0.15$ were prepared from zirconium *n*-propoxide (ZnP, $Zr(OC_3H_7)_4$ from Merck) and praseodymium acetylacetonate ($Pr(acac)_3$, $PrC_{15}H_{24}O_6$, Merck) by the following synthetic procedure. First, the ZnP was dissolved in a solution of 1-propanol (n-PrOH) to which was previously added acetylacetone (acac, $C_5H_8O_2$, Merck & Co.). That step was realized in nitrogen atmosphere to avoid fast hydrolysis and condensation of ZnP leading to precipitation. To that solution was added the required amount of $Pr(acac)_3$. The resulting solution was poured into a closed polyethylene bottle and held at 60 °C overnight. The formed gels were first dried at 60 °C during several hours and then at 120 °C. Finally, dried gels were annealed at different temperatures over the temperature range between 400 º and 1,300 °C for different times.

Structural and microstructural characterization of $Pr_xZr_{1-x}O_2$ samples

The chemical, structural, and microstructural features of prepared specimens were examined using different techniques. XRD analysis of powder samples (Model AXS D-5005, Bruker) was performed using a graphite monochromatic CuK_α radiation. The diffractometer had two 1º divergence slits, the scatter and receiving slits being 1º and 0.05º, respectively. The X-ray powder diffraction patterns were performed with a step size of 0.02 2θº and a counting time of 10 s. The determination of the lattice constants of zircon was made using the DICVOL indexing program. Infrared spectra (IR) of the specimens (Model 320 Avatar, Nicolet) were carried out in the range between 2,000 and 400 cm^{-1} by diluting the powder of specimens in KBr. Ultraviolet–visible (UV–vis) spectra of the specimens (Model V-670, Jasco) were obtained using the diffuse reflectance technique in the range of 200 to 2,500 nm using a $BaSO_4$ plate as the reflectance standard. The size and shape of the final nanoparticles were observed by transmission electron microscopy (TEM) at 100 kV (Model 1010, Jeol, Tokyo, Japan). Samples were prepared by

dispersing as-produced powders in absolute ethanol and setting dropwise on copper grids that had previously been coated with a holey thin carbon film.

Modified electrode preparation and electrochemical techniques

Paraffin-impregnated graphite electrodes (PIGEs) consist of cylindrical rods of 5-mm-diameter graphite impregnated under vacuum by paraffin as described by Scholz et al. [19]. To prepare sample-modified PIGEs, 0.1–1 mg of the material was powdered in an agate mortar and pestle and placed on a glazed porcelain tile, forming a spot of finely distributed material and then abrasively transferred to the surface of a PIGE by rubbing the electrode over that spot of the sample. Electrochemical experiments were performed at 298 K in a three-electrode cell under argon atmosphere using AgCl (3M NaCl)/Ag reference electrode and a platinum wire auxiliary electrode. Cyclic and square wave voltammograms (CVs and SWVs, respectively) were obtained with CH I420 potentiostat. Semi-derivative convolution of data was performed in order to increase peak resolution. In addition, 0.50 M sodium acetate/acetic acid and 0.50 M potassium phosphate (Panreac reagents) aqueous solutions were taken as electrolytes. Electrocatalytic experiments were carried out in 0.5–5.0 mM $NaNO_2$ (Panreac) solutions in acetate buffer. Photoelectrochemical experiments were performed alternating between dark conditions, obtained by confining the electrochemical cell within a BAS CE-2 box, and illumination conditions, obtained upon exposing the cell to direct illumination with a conventional 60 W lamp perpendicularly aligned with respect to the surface of the working electrode. Since the effect of light can be some heating of the graphite substrate followed by thermal (convective, enhanced diffusion) effects, the lamp was 1.0 m far from the electrochemical cell. SECM experiments were performed in a conventional four-electrode cell with CH 920c equipment. The bipotentiostat mode was used to apply potentials to the tip (E_T) and the electrode substrate (E_S). A microdisk platinum electrode tip (∅ 20 μm, CH 49) was used. Since graphite electrodes provide heterogeneous surfaces, for SECM measurements the substrate electrode was a Pt disk (geometrical area 0.018 cm^2), the reference electrode being again AgCl (3M NaCl)/Ag. The rate of scanning of the tip over the substrate was 40 μm/s for all measurements. Experiments were performed in previously deaerated 0.10–1.0 M NaOH and 2.0 mM $NaNO_2$ + 0. 50 M potassium phosphate buffer (Panreac) at pH 7.0. Microparticulate deposits of the undoped and doped zirconias over the substrate Pt electrode were obtained by evaporation of suspensions (ca. 0.1 mg/mL) of the corresponding specimens in ethanol previously ultrasonicated for 15 min.

Results and discussion

Characterization of $Pr_xZr_{1-x}O_2$

X-ray powder diffraction patterns of gels $Pr_{0.02}Zr_{0.98}O_2$ and $Pr_{0.10}Zr_{0.90}O_2$ after annealing at different temperatures are shown in Figs. 1 and 2, respectively. As can be seen, at 450 °C a phase with the structure of tetragonal ZrO_2 (JCPD 17-0385) is formed over the range of the prepared compositions (Fig. 1). On increasing the annealing temperature, the transformation from the tetragonal to the monoclinic crystalline form takes place in a range of temperatures, and at 1,100 °C all samples display monoclinic patterns (JCPD 36-0420) as a mainly crystalline phase as well as a minor secondary phase with pyrochlore structure (JCPD 19-1021), $Pr_2Zr_2O_7$, for compositions with higher nominal Pr content than $x = 0.03$, i.e., $Pr_{0.03}Zr_{0.97}O_2$. With the lattice parameter of the $Pr_xZr_{1-x}O_2$ being $x = 0.02$ and 0.10, crystalline phases developed after thermal annealing at 450 and 1,300 °C are shown in Table 1. For both specimens, the tetragonal and monoclinic undoped phases have been included as reference for the ones doped with different amounts of Pr.

The IR spectra of praseodymium-containing zirconia gels $Pr_xZr_{1-x}O_2$, with $x = 0.00$, 0.02, 0.05, and 0.10, heated at 450 and 1,300 °C for 3 h are displayed in Fig. 3. In both specimens displaying a tetragonal structure, bands that peaked at 460 and 570 cm^{-1} can be attributed to the

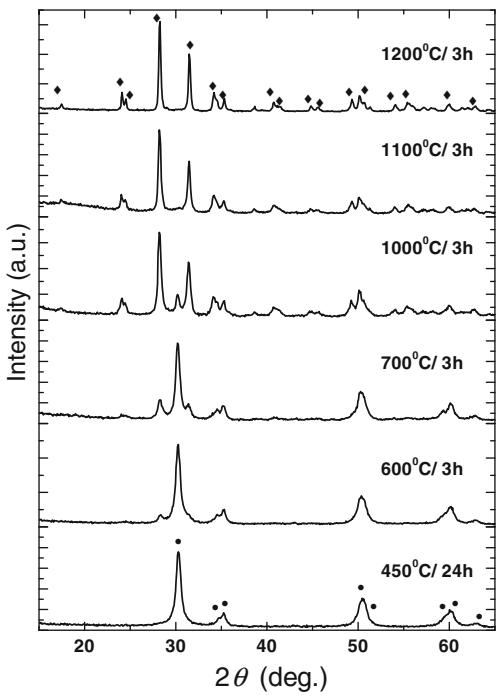

Fig. 1 X-ray powder diffraction pattern of gels $Pr_{0.02}Zr_{0.98}O_2$ annealed at different temperatures and/or heating times (*filled diamond* is monoclinic zirconia; *filled circle* is tetragonal zirconia)

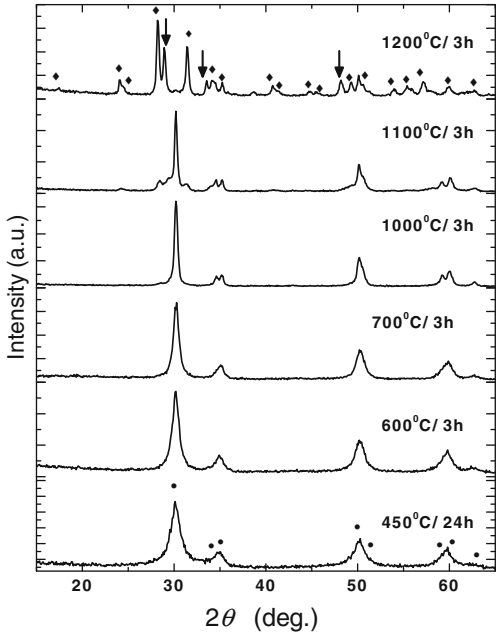

Fig. 2 X-ray powder diffraction pattern of gels $Pr_{0.10}Zr_{0.90}O_2$ annealed at different temperatures and/or heating times (*filled diamond* is monoclinic zirconia, *filled circle* is tetragonal zirconia, and *down arrow* is $Pr_2Zr_2O_7$)

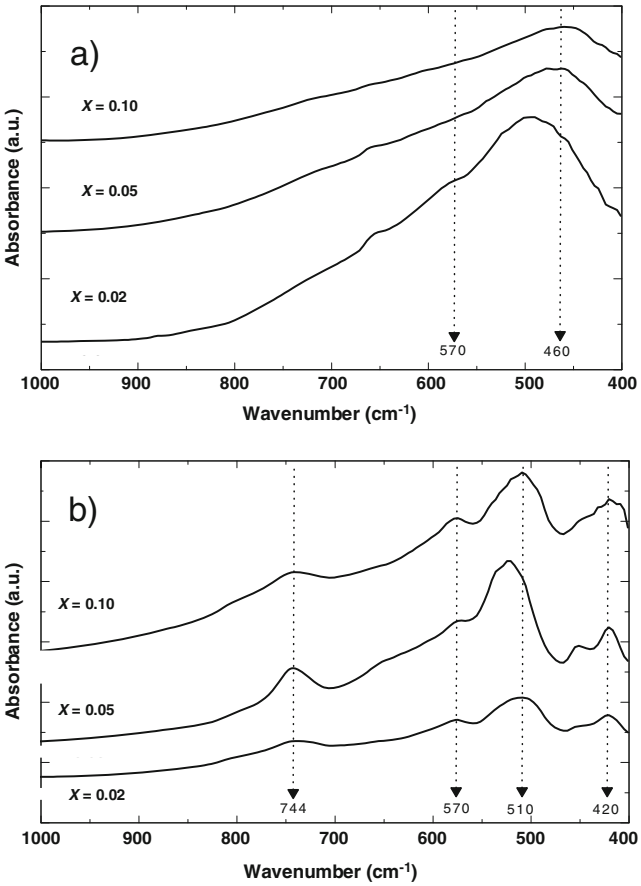

Fig. 3 IR spectra of **a** tetragonal and **b** monoclinic $Zr_{1-x}Pr_xO_2$, with $x = 0.02$, 0.05, and 0.10

stretching modes of the Zr–O bond [43]. For the specimens heated at 1,300 °C, whose diffraction patterns confirm the formation of monoclinic Pr-containing ZrO_2 solid solutions, the IR bands appear at around 744, 570, 510, 448, and 420 cm^{-1}, which have also been attributed to the Zr–O bonds [44].

Diffuse reflectance spectra of undoped zirconia and doped compositions with $x = 0.00$, 0.02, and 0.10 heated at the chosen temperatures are shown in Fig. 4. In both solid solutions, crystalline forms appear as a strong, narrow band at around 270 nm and a high-intensity, wide band also peaked at around 330 nm, which is decreasing monotonically in intensity up to 600 nm. Additionally, the absorption spectra of Pr-doped ZrO_2 samples display two sets of narrow, weak bands over the ranges 1,350–1,550 and 1,700–1,900 nm, respectively. However, other bands in the 440–610-nm range associated with 4f inter-level electronic transitions in Pr^{3+} ion are not distinguished in the spectra trace of our prepared samples [12, 13]. In order to assign the observed bands to the electronic transitions yielded by the Pr cation in the available structural sites in the zirconia lattices, some comment on the results previously obtained by different authors is worthwhile. Thus, Ramos-Brito et al. [12, 13] reported the diffuse reflectance spectra for praseodymium-doped zirconia powders as a function of the relative amount of praseodymium with respect to the zirconium in the starting precursors. The diffuse reflectance spectra of these $Pr_xZr_{1-x}O_2$ solid

Table 1 Lattice parameters of samples $Pr_xZr_{1-x}O_2$ specimens annealed at 450 and 1,300 °C/3 h. In parenthesis is the standard deviation in the last significant figure

x	*a*=*b* (Å)	*a* (Å)	*b* (Å)	*c* (Å)	*V* (Å^3)
At 450 °C/3 h					
0.0	3.599 (1)			5.167 (1)	67.03 (1)
0.02	3.59987 (1)			5.17572 (1)	67.072 (1)
0.1	6.60980 (1)			5.19177 (1)	67.652 (1)
At 1,300 °C/3 h					
0.0		5.1508 (1)	5.2016 (1)	5.315 (1)	140.58 (1)
0.02		5.15629 (1)	5.20380 (1)	5.31937 (1)	140.935 (1)
0.1		5.16111 (1)	5.20793 (1)	5.32242 (1)	141.305 (1)

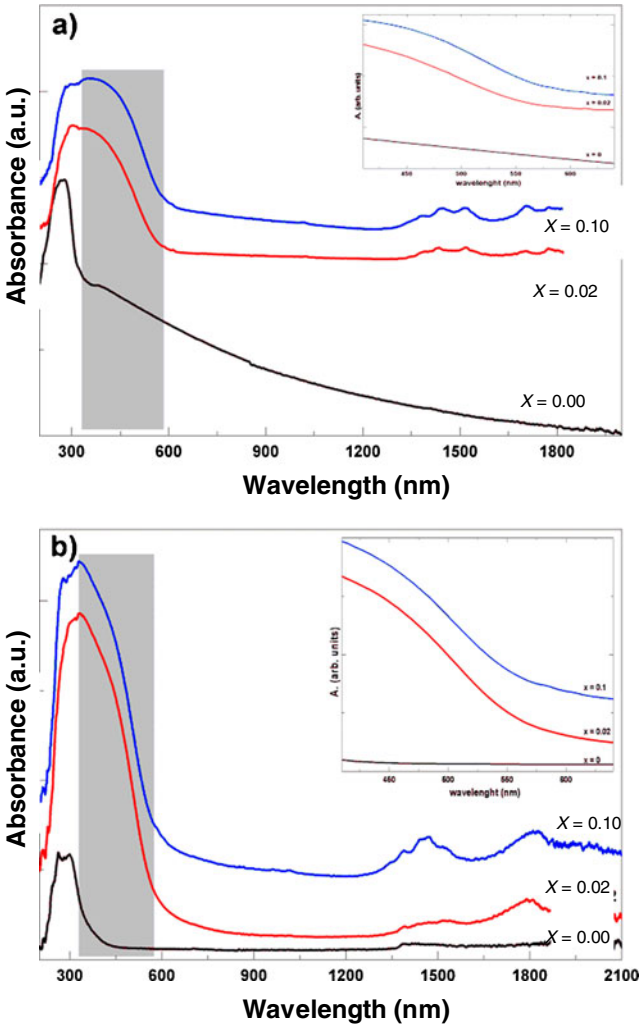

Fig. 4 Diffuse reflectance spectra of $Pr_xZr_{1-x}O_2$, with $x = 0$, 0.02 and 0.10: **a** tetragonal, **b** monoclinic

solutions, obtained by thermally processing the precursors, displayed for samples with low concentration of praseodymium a wide absorption band centered at 380 nm with a constant intensity. For a higher amount of dopant, the intensity of this band starts to lower and a new band appeared at around 295 nm. The first wide band at 380 nm was attributed to deep energy levels in zirconia energy gap caused by the creation of crystal defects with the incorporation of Pr^{3+} while the second at around 295 nm was associated with 4f→5d absorption of Pr^{3+}. Additional bands were also reported in the region of 440–610 nm which were associated with the electronic transitions within the 4f shell of Pr^{3+} ions. All of these results on the absorption spectra of these $Pr_xZr_{1-x}O_2$ specimens obtained by co-precipitation indicate that praseodymium into the ZrO_2 host lattice was in the +3 chemical state. In the same sense, Suchroski et al. [10], on the basis of a XPS study, concluded recently that Zr^{4+} and Pr^{3+} are the main oxidation states in zirconia nanopowders doped with Pr_2O_3. However, prior studies have suggested the feasibility to stabilize Pr^{4+} in several host lattices. In fact, the widely used industrially yellow ceramic pigment $Pr_xZr_{1-y}Si_{1-z}O_4$ ($y + z = x$) is a solid solution of Pr^{4+} in the zircon host lattice as it has been proved by different authors [45]. Recently, Pawlak et al. [14] reported absorption bands in the 430–500-, 570–620-, and 960–1,040-nm regions for $(Y_{1-x-y}Pr_xMg_y)_3Al_5O_{12}$ ($x = 0.012$, $y = 5 \times 10^{-6}$) materials annealed in oxidizing (air) or reducing atmospheres (hydrogen/nitrogen). The spectra of both samples exhibited the characteristic absorption lines of Pr^{3+}. However, the absorption spectrum of specimens annealed under oxidizing atmosphere contained additional broad features in the 300–570-nm region. This absorption has been associated with the 4f → 5d transitions of Pr^{4+} [46, 47]. Although an attempt was made to detect luminescence from Pr^{4+} in these specimens, emission was detected only from Pr^{3+}. The lack of Pr^{4+} luminescence can be explained by the energy transfer from Pr^{4+} to Pr^{3+} [14].

The absorption spectra of our prepared specimens $Pr_xZr_{1-x}O_2$, $0 \le x \le 0.15$, in which there is a broad and intense absorption in the range 370–600 nm, give evidence on the presence of Pr^{4+}, even for specimens with the higher nominal content of Pr in which the excess of Pr as structural cation in the pyrochlore crystalline phase, $Pr_2Zr_2O_7$, is present. Therefore, the feasibility of stabilization of the +4 chemical state of Pr as well as the presence of a relatively small amount of Pr^{3+} in the ZrO_2 host lattice can be assumed.

TEM micrographs of the prepared specimens $Pr_{0.02}Zr_{0.98}O_2$ and $Pr_{0.10}Zr_{0.90}O_2$ are shown in Figs. 5 and 6, respectively. As can be seen in Fig. 7, the nanoparticles of both crystalline forms display sizes smaller than 15 nm if $x = 0.10$, while for the tetragonal form and $x = 0.02$ the particles are larger, up to 60 nm. The difference in sizes can be understood because higher annealing temperatures are required to stabilize nanoparticles in the monoclinic form, hence favoring grain growth.

Electrochemistry of undoped zirconias

Figure 8 compares CVs for graphite electrodes modified with m-ZrO_2 in contact with 0.50 M aqueous potassium phosphate buffer at pH 7.0 upon scanning the potential from the open-circuit potential in the (a) negative and (b) positive directions. In the first case, three overlapping cathodic waves at potentials of −0.20 (I), −0.46 (II), and −0.70 V (III) vs. AgCl/Ag are obtained, followed, in the subsequent anodic scan, by overlapping anodic waves at ca. −0.20 (III′), +0.10 (II′) and +0.25 (III′) V. In the initial anodic scan voltammogram, there are no oxidation peaks during the first scan, the voltammetric response from the subsequent cathodic scan being identical to that recorded for the initial cathodic scan

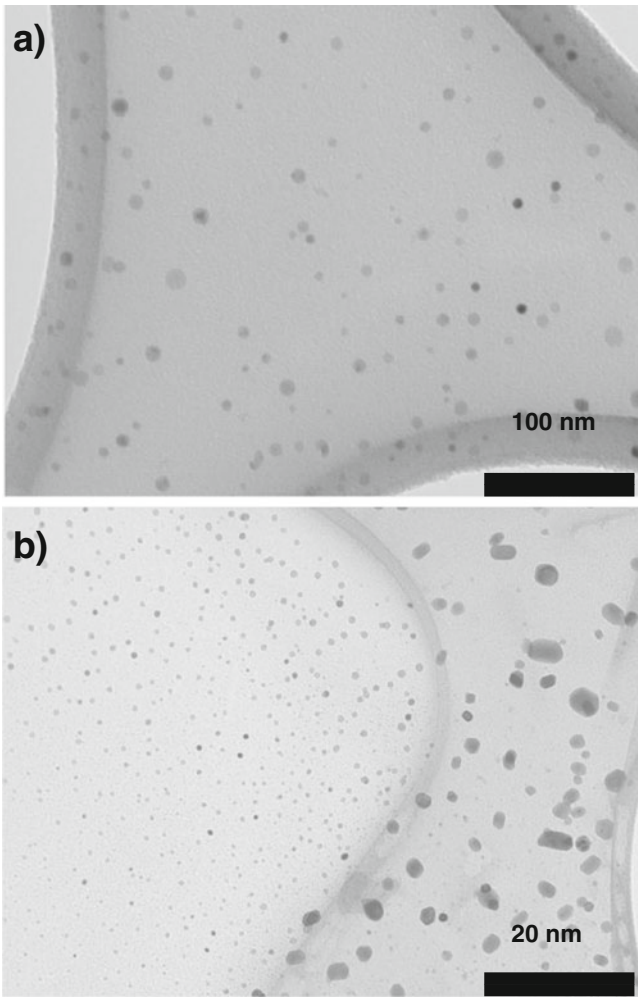

Fig. 5 TEM micrographs of $Pr_xZr_{1-x}O_2$ nanoparticles, with $x = 0.02$, annealed at: **a** 450 °C (tetragonal form), **b** 1,300 °C (monoclinic form)

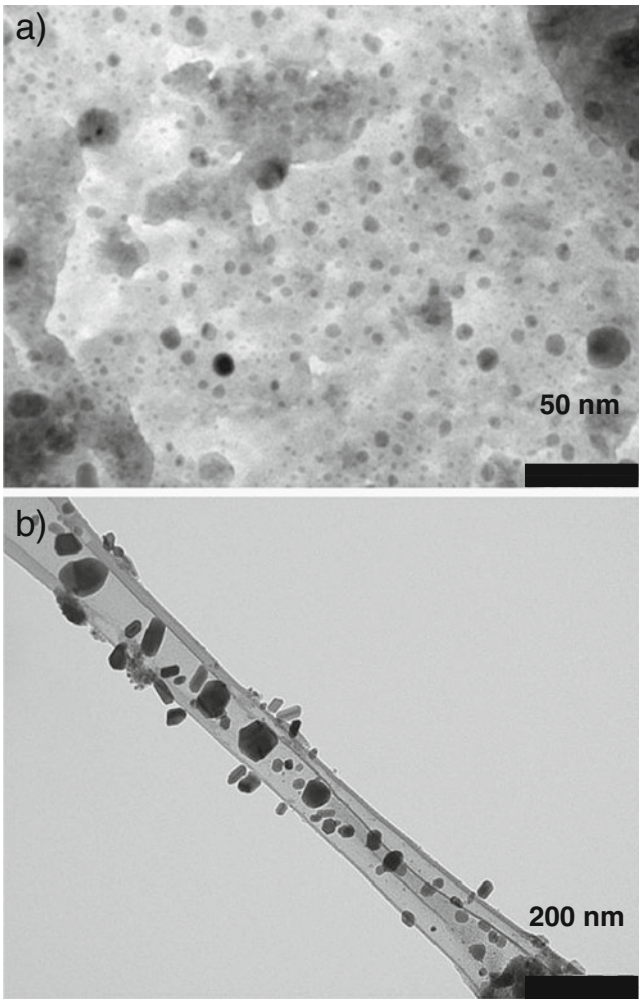

Fig. 6 TEM micrographs of $Pr_xZr_{1-x}O_2$ nanoparticles, with $x = 0.10$, annealed at: **a** 450 °C (tetragonal form), **b** 1,300 °C (monoclinic form)

voltammograms. These features clearly suggest that zirconium is initially in its +4 oxidation state. The voltammetry of t-ZrO_2 was essentially identical. The peak potentials (E_p) are negatively shifted on increasing pH and positively shifted on increasing square wave frequency. Linear E_p vs. pH plots were obtained for experiments in acetate and phosphate buffers at pH values between 4.0 and 8.0. The slope of such representations for all peaks was 55±10 mV/decade, suggesting, in agreement with literature for the electrochemistry of transition metal oxides [48–50], that equal numbers of protons and electrons are involved. Although the standard potential for the process

$$Zr^{IV}O_2(s) + 4H^+ + 4e^- \rightarrow Zr + 2H_2O \quad (1)$$

(−1.45 V vs. SHE; [51]) would make it possible that a complete reduction to Zr could occur, it is more reasonable to assume a stepwise reduction of the zirconia similar to what has been observed for Ru oxide [52]. The observed rather reversible behavior denotes that the structure of the parent oxide is not seriously affected so that the reduction of zirconias can be described either as a stepwise reduction to different suboxides or the reduction to one suboxide but of differently sized particles. The appearance of different signals may also be due to differently sized nanoparticles and nanoparticle aggregates [53] or even to the relatively large heterogeneity in the shape and size distribution of zirconia grains, a frequent effect in the voltammetry of microparticles, as described for the reduction of iron oxides and related materials by Grygar [54, 55]. Further, it is possible that the reduction process occurs only at the three-phase junction graphite–zirconia–solution and does not penetrate deeply into the zirconia particles. This situation would be similar to that described by Falgairette et al. [56] for the reduction of zirconia at Pt/yttrium-stabilized zirconia interfaces. The partial reduction of zirconia is also supported by the observation that it is impossible to observe the formation of Zr even when very negative potentials are applied. Consistently, there is considerable difficulty to

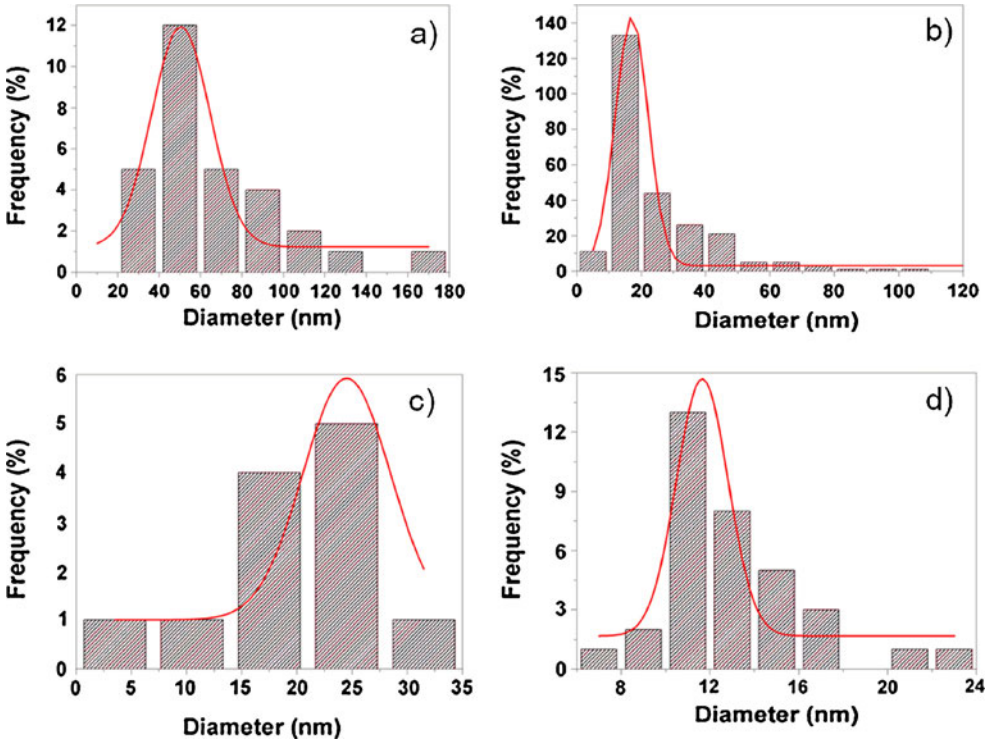

Fig. 7 Histograms corresponding to the size distribution of $Pr_xZr_{1-x}O_2$ nanoparticles annealed at: **a**, **b** 450 °C (tetragonal); **c**, **d** 1,300 °C (monoclinic); $x = 0.02$ for **a**, **c** and $x = 0.1$ for **b**, **d**

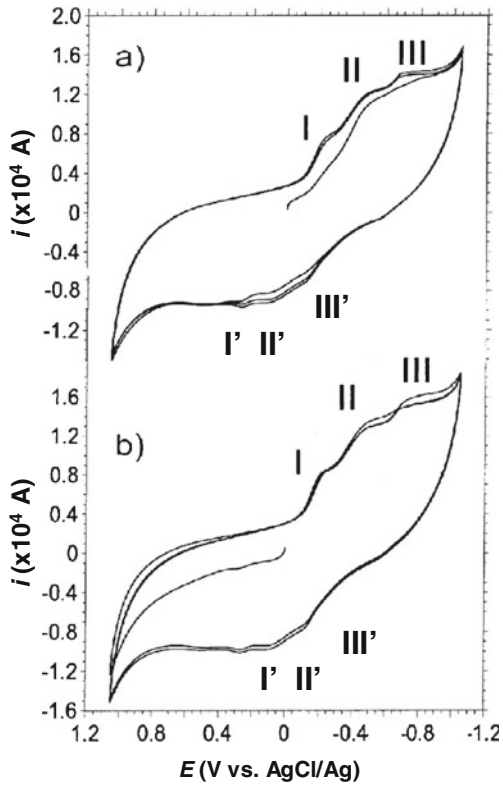

Fig. 8 CVs for m-ZrO_2-modified PIGEs immersed into 0.50 M potassium phosphate buffer at pH 7.0. Potential scan rate 50 mV/s. Potential scan initiated at +0.25 V in the **a** negative and **b** positive directions

reduce ZrO_2 under molten salt conditions at high temperatures [57].

Electrochemistry of $Pr_xZr_{1-x}O_2$ materials

The voltammetric response of t-$Pr_xZr_{1-x}O_2$ and m-$Pr_xZr_{1-x}O_2$ specimens was in principle similar to that of t-ZrO_2 and m-ZrO_2, respectively, but additional features, which can be associated to Pr centers, appear. This can be seen on comparing the SWVs in Fig. 9 for m-ZrO_2 and t-ZrO_2 with those in Fig. 10 for m-$Pr_{0.03}Zr_{0.97}O_2$ and m-$Pr_{0.10}Zr_{0.90}O_2$ attached to PIGEs in contact with aqueous phosphate buffer. Undoped zirconias show peaks at −0.10 (I), −0.48 (II), and −0.67 V (III), in agreement with CV records in Fig. 8. For Pr-containing specimens, additional peaks at +0.21 (IV) and −0.58 V (V) are recorded. Peaks IV and V remain frequency independent in the 2–500-Hz frequency range, thus suggesting an essentially reversible behavior. Similar features were obtained for the corresponding tetragonal materials. The height of peaks IV and V increases significantly on increasing the Pr content and can be attributed, respectively, to the Pr(IV)/Pr(III) and Pr(III)/Pr(II) redox couples (vide infra), although the recorded potentials are far from those calculated for the Pr^{4+}/Pr^{3+} (+3.2 V vs. SHE) and Pr^{3+}/Pr^{2+} (−2.35 V vs. SHE) couples in solution phase [51, 58].

To discriminate the oxidation state of a system containing a reversibly reducible/oxidizable electroactive species in two oxidation states, one can use the reported voltam-

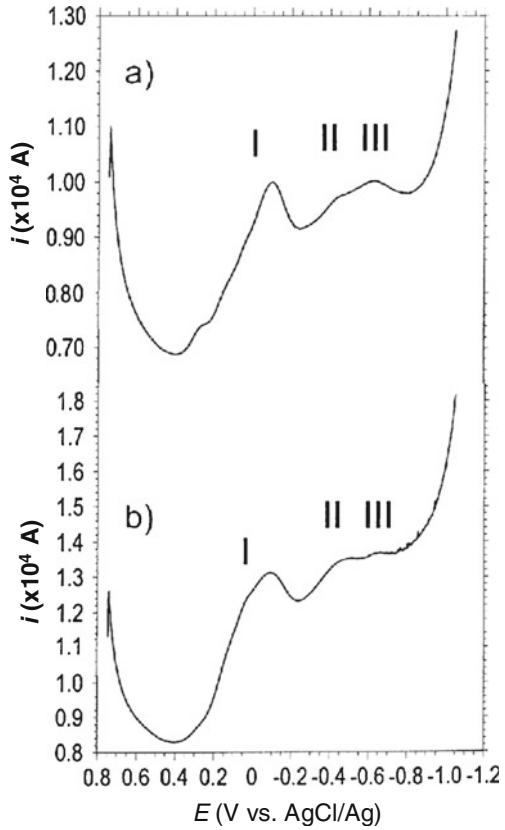

Fig. 9 SWVs of PIGEs modified with **a** m-ZrO_2, **b** t-ZrO_2, immersed into 0.50 M potassium phosphate buffer (pH 7.0). Potential scan initiated at +0.75 V in the negative direction. Potential step increment 4 mV; square wave amplitude 25 mV; frequency 5 Hz

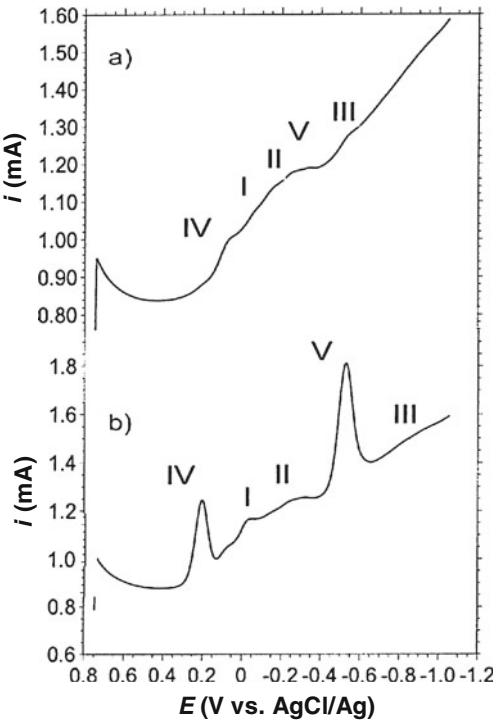

Fig. 10 SWVs for **a** m-$Pr_{0.03}Zr_{0.97}O_2$ and **b** m-$Pr_{0.10}Zr_{0.90}O_2$ attached to PIGEs in contact with 0.50 M potassium phosphate buffer (pH 7.0). Potential scan initiated at +0.75 V in the negative direction. Potential step increment 4 mV; square wave amplitude 25 mV; frequency 50 Hz

metric methods [59–61] requiring, in principle, linear diffusion control and electrochemical reversibility. The application of such methods to solid materials is, in principle, possible because of the close similarity between the CV responses for species in solution phase and for ion insertion solids when reversibility exists [62]. The application of the peak current method [60, 61] to processes IV and V is illustrated in Fig. 11. Simulation of CVs for species in solution indicates that, when the cyclic voltammogram is initiated at the midpeak potential of the involved reversible couple, the quotient between the anodic peak current in the first (i_{pa}(I)) and second (i_{pa}(II)) scans becomes proportional to the molar fraction of oxidized (or reduced) species α_{ox}:

$$i_{pa}(I)/i_{pa}(II) - Xa_{ox} + Y \quad (2)$$

In the above equation, X and Y represent numerical coefficients depending on the potential scan rate and the separation between the switching potentials. In practice, however, CVs for microparticulate deposits exhibit large resistive and capacitive effects seriously distorting the voltammograms. The reversible behavior can be seen in Fig. 11 (inset) for m-$Pr_{0.10}Zr_{0.90}O_2$ immersed into phos-

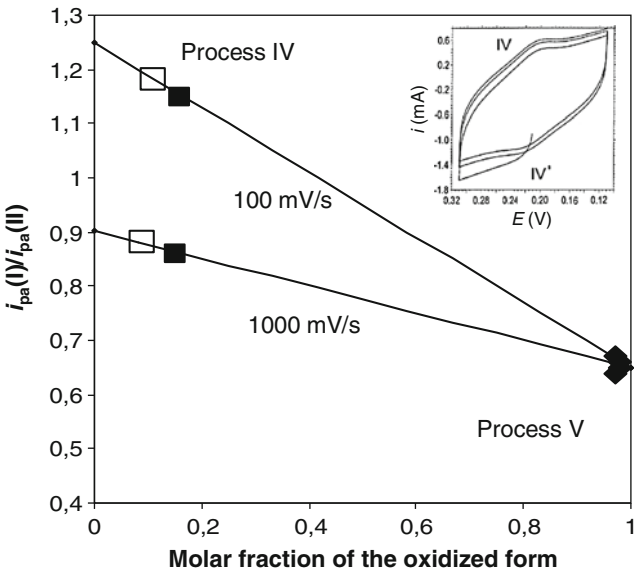

Fig. 11 Values of the i_{pa}(I)/i_{pa}(II) ratio for processes IV (*squares*) and V (*rhombs*) for samples m-$Pr_{0.03}Zr_{0.97}O_2$ (*empty figures*) and m-$Pr_{0.10}Zr_{0.90}O_2$ (*solid figures*) and position in the theoretical i_{pa}(I)/i_{pa}(II) vs. α_{ox} diagram obtained for CVs initiated at the midpoint potential for a one-electron reversible couple at potential scan rates of 100 and 1,000 mV/s. *Inset*, repetitive CV for m-$Pr_{0.10}Zr_{0.90}O_2$-modified PIGEs immersed into 0.50 M potassium phosphate buffer. The CVs were initiated at the midpeak potential of the IV/IV' couple in the positive direction. Potential scan rate 100 mV/s

phate buffer. Here, repetitive CV initiated at the midpeak potential for process IV in the positive direction is shown. An easy correction of such effects can be obtained in the studied case, merely by subtracting the CV recorded for the corresponding non-doped m- or t-ZrO_2. Using corrected peak currents, the $i_{pa}(I)/i_{pa}(II)$ ratio provides values of α_{ox} = 0.09±0.04 for m-$Pr_{0.03}Zr_{0.97}O_2$ and α_{ox} = 0.12±0.04 for $Pr_{0.10}Zr_{0.90}O_2$ for process IV (see Fig. 11). Consistently, similar α_{ox} values were obtained for each material using potential scan rates of 100, 200, 500, and 1,000 mV/s. For the process V, both $Pr_{0.03}Zr_{0.97}O_2$ and $Pr_{0.10}Zr_{0.90}O_2$ materials displayed an essentially identical response at all scan rates, corresponding to α_{ox} = 1.00±0.04; i.e., there is no Pr in its +2 oxidation state in the original samples.

The results obtained for electrochemical signals IV and V indicate that the praseodymium species responsible for such processes is in the +3 oxidation state in the studied materials and can be associated to the pyrochlore crystalline phase, $Pr_2Zr_2O_7$, increasingly present in specimens upon increasing the Pr loading. Subtractive voltammetry, however, provides a more complicated picture. As shown in Fig. 12, subtracting SWVs for m- and t-$Pr_xZr_{1-x}O_2$ specimens with low praseodymium loadings from those recorded for m- and t-ZrO_2 materials, respectively, reveals additional voltammetric peaks. Here, voltammetric peaks at +0.09 (VI), −0.06 (VII), and −0.15 V (VIII) appear for m-$Pr_xZr_{1-x}O_2$ specimens while only peaks at +0.07 (VI) and −0.14 V (VIII) are recorded for t-$Pr_xZr_{1-x}O_2$ probes. All these features can be rationalized on assuming that, at low praseodymium loadings, Pr^{4+} centers are incorporated to the zirconia matrix, thus producing electrochemical processes VI–VIII with differences between monoclinic and tetragonal materials. The stepwise reduction of such Pr(IV) centers can tentatively be represented as:

$$Pr^{IV}{}_xZr_{1-x}O_2(s) + xH^+(aq) + xe^- \rightarrow Pr^{III}{}_xZr_{1-x}O_{2-x}(OH)_x(s) \quad (3)$$

$$Pr^{III}{}_xZr_{1-x}O_{2-x}(OH)_x(s) + xH^+(aq) + xe^- \rightarrow Pr^{II}{}_xZr_{1-x}O_{2-2x}(OH)_{2x}(s) \quad (4)$$

On increasing praseodymium loadings, the voltammetric response is dominated by peaks IV and V attributable to a Pr (III)-pyrochlore phase accompanying zirconias. This is oxidized to Pr(IV) via process IV (notice that square wave voltammograms equally present oxidation and reduction peaks) and reduced to Pr(III) via process V. These processes can formally be represented as:

$$Pr^{III}{}_2O_3(s) + 2OH^- \rightarrow 2Pr^{IV}O_2(s) + H_2O + 2e^- \quad (5)$$

$$Pr^{III}{}_2O_3(s) + 2H^+(aq) + 2e^- \rightarrow 2Pr^{II}O(s) + H_2O \quad (6)$$

Electrocatalytic effects

In order to obtain additional information on the role of praseodymium centers in the electrochemistry of t- and m-$Pr_xZr_{1-x}O_2$ materials, catalytic effects on the oxygen evolution reaction and nitrite reduction were performed.

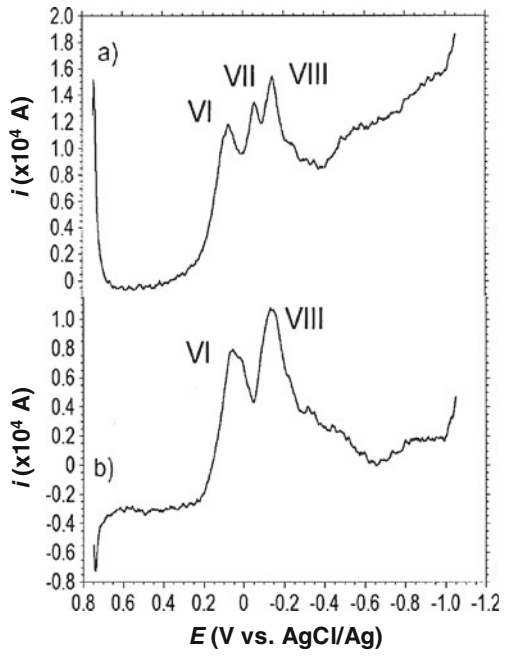

Fig. 12 Deconvolution of subtracted voltammograms for **a** m-$Pr_{0.03}Zr_{0.97}O_2$ minus m-ZrO_2 and **b** t-$Pr_{0.03}Zr_{0.97}O_2$ minus t-ZrO_2. Electrolyte: 0.50 M sodium acetate buffer (pH 4.75). Potential scan initiated at +0.75 V in the negative direction. Potential step increment 4 mV; square wave amplitude 25 mV; frequency 5 Hz

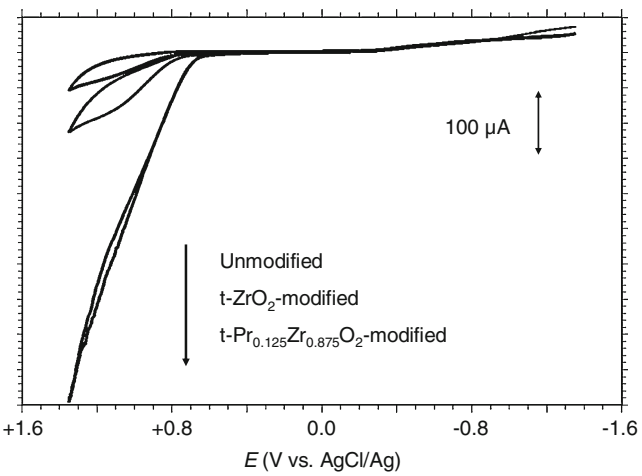

Fig. 13 CVs at unmodified, t-ZrO_2-modified, and t-$Pr_{0.125}Zr_{0.875}O_2$-modified graphite electrodes immersed into 1.0 M NaOH. Potential scan rate 20 mV/s

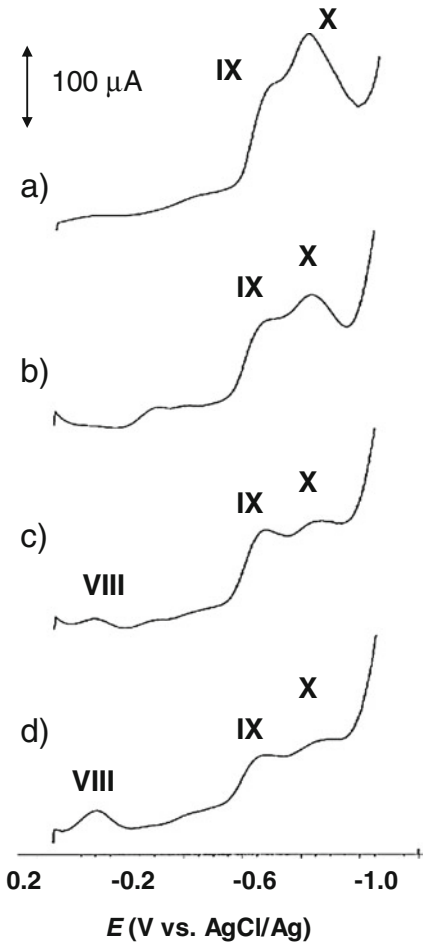

Fig. 14 SWVs for a 2.0 mM $NaNO_2$ solution in 0.50 M aqueous sodium acetate buffer (pH 4.75) at **a** bare PIGE, **b** m-ZrO_2-, **c** m-$Pr_{0.03}Zr_{0.97}O_2$-, and **d** m-$Pr_{0.05}Zr_{0.95}O_2$-modified PIGEs. Potential scan initiated at +0.05 V in the negative direction. Potential step increment 4 mV; square wave amplitude 25 mV; frequency 5 Hz

As can be seen in Fig. 13, the currents for the OER at potentials above +1.0 V are significantly enhanced at ZrO_2-modified electrodes with respect to the unmodified ones. This effect is considerably larger for t- and m-$Pr_xZr_{1-x}O_2$ materials relative to the corresponding undoped zirconias and can in principle be described, following literature [63–65], in terms of the association between the substrate and the catalyst in high oxidation state (typically, RuO_2, IrO_2):

$$M^{IV} + OH^- \rightarrow M^{IV}OH + e^- \quad (7)$$

$$M^{IV}OH + OH^- \rightarrow M^{IV}O + H_2O + e^- \quad (8)$$

$$2M^{IV}O \rightarrow 2M^{IV} + O_2 \quad (9)$$

The appearance of large catalytic effects for t- and m-$Pr_xZr_{1-x}O_2$ materials would support the idea that Pr centers are mainly in the +4 oxidation state.

Figure 14 compares SWVs for a 2.0-mM $NaNO_2$ solution in 0.50 M aqueous acetate buffer at a bare PIGE electrode and at m-ZrO_2, m-$Pr_{0.03}Zr_{0.97}O_2$-, and m-$Pr_{0.05}Zr_{0.95}O_2$-modified PIGEs. At the unmodified graphite electrode, two overlapping reduction peaks at −0.68 (IX) and −0.80 V (X) appear. At m-ZrO_2, the relative height of such peaks varies while the rising current appearing at potentials more negative than −1.0 V increases significantly. At m-$P_xZr_{1-x}O_2$-modified PIGEs, the voltammetric response becomes essentially unchanged except for the appearance of an additional peak at −0.10 V. The potential of this peak is close to that of peak VIII recorded at $Pr_xZr_{1-x}O_2$ probes, and the peak current is enhanced on increasing the Pr loading as well as the concentration of nitrite. The enhancement of the Pr-centered peak can be interpreted in terms of the catalytic effect of praseodymium centers on nitrite reduction, similarly to electrocatalytic processes using polyoxometalate systems [65]. The intensity of these peaks remains essentially unchanged for praseodymium loadings larger than x = 0.05, thus suggesting that the catalytic effect is exclusively (or, at least, mainly) associated to praseodymium centers in the zirconia phases rather than pyrochlore. Consistently, the intensity of pyrochlore-centered peaks IV and V remain independent on nitrite concentration.

SECM data provide confirmation for the observed electrocatalytic effect, as depicted in Fig. 15 for deposits

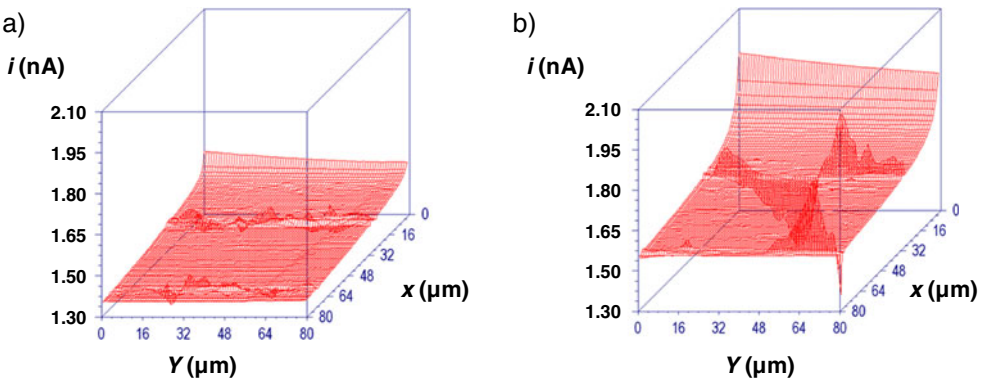

Fig. 15 SECM topographic image recorded for a microparticulate deposit of **a** m-ZrO_2 and **b** m-$Pr_{0.05}Zr_{0.95}O_2$ immersed into 2.0 mM $NaNO_2$ + 0.25 M potassium phosphate buffer (pH 7.0). E_T = −0.65 V; E_S = −0.65 V

of m-ZrO_2 and $Pr_{0.05}Zr_{0.95}O_2$ in contact with a $NaNO_2$ solution in phosphate buffer. To promote clearer differences between ZrO_2 and $Pr_xZr_{1-x}O_2$ specimens, a strategy where the tip competes with the substrate for the very sample analyte, equivalent to that termed redox competition scanning electrochemical microscopy, recently employed by several authors [66, 67], was used. Under the conditions in Fig. 15, the tip current for Pr-doped specimens presents peaks considerably larger than those obtained for undoped zirconias, in agreement with the aforementioned catalysis associated to Pr centers. Here, a potential sufficiently negative (−0.65 V) to promote the reduction of nitrite at the substrate electrode is applied so that tip current peaks appear when the tip is held at a potential similar to that of the substrate (−0.65 V). This can be interpreted on assuming that electrocatalysis involves as a first step the electrochemical reduction of Pr(IV) centers and its regeneration by reaction with nitrite similarly to, for instance, hydrogen evolution reaction catalyzed by heteropolyanions/carbon nanotubes hybrid material [68]. The reaction scheme can be represented as:

$$Pr^{4+} + e^- \rightarrow Pr^{3+} \quad (10)$$

$$NO_2^- + 2H^+ + Pr^{3+} \rightarrow NO + H_2O + Pr^{4+} \quad (11)$$

Figure 16 illustrates schematically the possible catalytic cycle which requires the reversibility of the Pr^{4+}/Pr^{3+} couple. Interestingly, the electrocatalytic pattern of m-$P_xZr_{1-x}O_2$ materials changed upon illumination. As can be seen in Fig. 17, on exposing the electrode to visible light illumination, the peak VIII disappears. The disappearance of this peak is correlated with the loss of catalytic activity as monitored by SECM experiments under sequentially interrupted illumination. This can be seen in Fig. 18 where

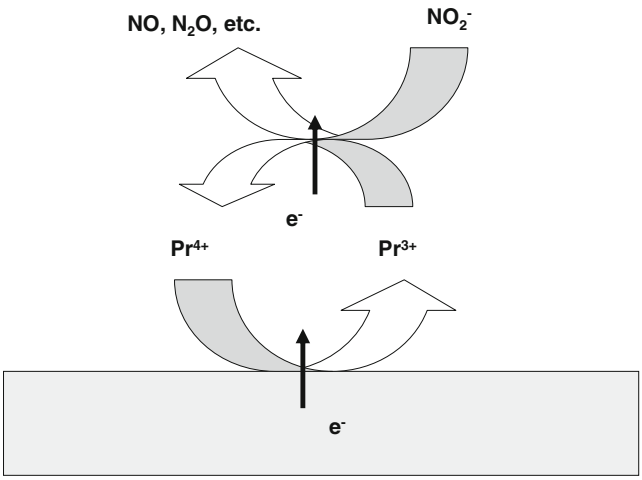

Fig. 16 Schematics for the electrocatalytic effect of m- and t-$Pr_xZr_{1-x}O_2$ on nitrite reduction in aqueous media

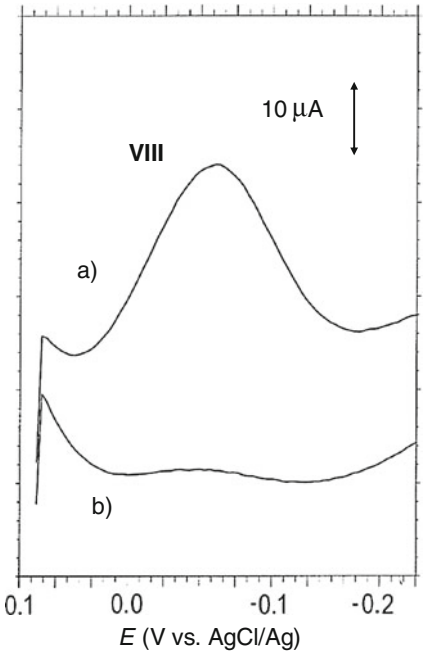

Fig. 17 SWVs for a 2.0 mM $NaNO_2$ solution in 0.50 M aqueous sodium acetate buffer (pH 4.75) at a m-$Pr_{0.10}Zr_{0.90}O_2$-modified PIGE (*a*) under dark conditions and (*b*) under illumination. Potential scan initiated at +0.05 V in the negative direction. Potential step increment 4 mV; square wave amplitude 25 mV; frequency 5 Hz

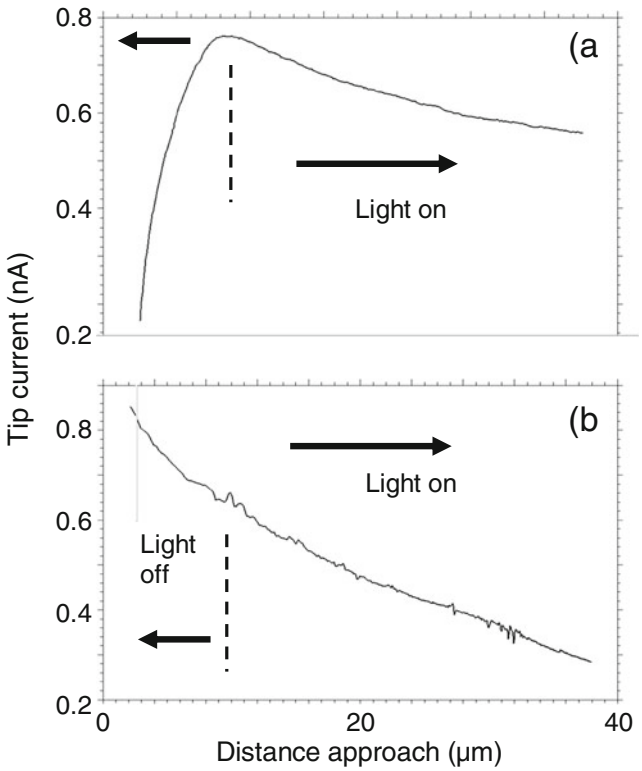

Fig. 18 Probe approach curves recorded for microparticulate deposits of (**a**) m-$Pr_{0.10}Zr_{0.90}O_2$ and (**b**) m-ZrO_2 immersed into 2.0 mM $NaNO_2$ + 0.25 M potassium phosphate buffer (pH 7.0). E_T = −0.65 V; E_S = −0.65 V upon alternating steps of darkness/illumination

the SECM probe approach curves obtained for the microparticulate deposits of m-ZrO_2 and m-$Pr_{0.10}Zr_{0.90}O_2$ immersed into 2.0 mM $NaNO_2$ + 0.25 M potassium phosphate buffer (pH 7.0) are shown. Alternative illumination/de-illumination of the cell during the record of the probe approach curve in SECM experiments determines drastic differences between undoped and Pr-doped materials, as can be seen in Fig. 18. While for the undoped material there is no apparent influence of the illumination and the tip current decreases monotonically on decreasing the distance (i.e., on increasing the distance approach) with the substrate, as expected for a nonconducting substrate, doped materials exhibit the opposite effect under dark conditions, with illumination restoring the nonconducting behavior. Apparently, illumination produces a negative electrocatalytic effect which can be associated to energy transfer from Pr^{4+} to Pr^{3+} following the absorption of radiation by Pr^{4+} [14]. As a result, the reversibility in the electrochemical regeneration of Pr^{4+} would become decreased and the catalytic cycle depicted in Fig. 16 blocked, but further research is needed to elucidate this matter.

Conclusions

An electrochemistry study of Pr-doped nanocrystals was performed to characterize praseodymium centers in Pr-doped tetragonal and monoclinic zirconias. Gels with compositions in the range $Pr_xZr_{1-x}O_2$, $0 \le x \le 0.15$ were prepared by controlled hydrolytic sol–gel process and annealed at different temperatures. XRD, IR, and UV–vis proved the formation of monoclinic and tetragonal Pr-containing ZrO_2 materials and gave evidences that a significant proportion of praseodymium cations were in (IV) oxidation state. TEM micrographs demonstrated that nanoparticulated solid solutions are sized at around 15 and 60 nm for tetragonal or monoclinic zirconia, respectively. The voltammetry and SECM study confirmed that a relatively high content of praseodymium cation was in the oxidation state (IV), i.e., as Pr^{4+}, in both zirconia host lattices.

Acknowledgments The authors thank the financial support from the Ministry of Science and Innovation through the program Consolider 2010 (Project CSD2010-00065) and MEC Project CTQ2006-15672-C05-05/BQU, supported with ERDF funds.

References

1. Narula CK, Allison JE, Bauer DR, Gandhi AMHS (1996) Chem Mater 8:984–1003
2. Badenes JA, Llusar M, Calbo J, Tena MA, Monrós G (2001) British Ceram Trans 100:251–255
3. Zhuykov S (2007) Electrochemistry of zirconia gas sensors. CRC, Boca Raton
4. Fidelus JD, Lojkowski W, Millers D, Grigorjeva L, Smits K, Piticescu RR (2007) Solid State Phenom 128:141–150
5. Naskar MK, Ganguli D (1996) J Mater Sci 31:6263–6267
6. Zhu J, van Ommen JG, Bouwmeester HJM, Lefferts J (2005) J Catal 233:434–441
7. Moon J, Choi H, Kim H, Lee C (2002) Surf Coat Tech 155:1–10
8. Chevalier J (2006) Biomaterials 27:535–543
9. Brahim C, Ringuede A, Cassir M, Putkonen M, Niinisto L (2007) Appl Surf Sci 253:3962–3968
10. Suchorski Y, Wrobel R, Becker S, Opalínska A, Narkiewicz U, Podsiadly M, Weiss A (2008) Acta Phys Polonica A 114:S125–S134
11. Corradi AB, Bondioli F, Ferrari AM (2001) Chem Mater 13:4550–4554
12. Ramos-Brito F, Murrieta H, Hernández SJ, Camarillo AE, García-Hipólito M, Martínez-Martínez R, Álvarez-Fragoso O, Falcony C (2006) J Phys D Appl Phys 30:2079–2083
13. Ramos-Brito F, Alejo-Armenta C, García-Hipólito M, Camarillo E, Hernández J, Murrieta AH, Falcony C (2008) Optical Mater 30:1840–1847
14. Pawlak D, Frukacz Z, Mierczyk Z, Suchocki A, Zachara J (1998) J Alloys Comp 361:275–277
15. Logan AD, Shelef M (1994) J Mater Res 9:468–475
16. O'Connell M, Morris MA (2000) Catal Today 59:387–393
17. Scholz F, Meyer B (1998) Voltammetry of solid microparticles immobilized on electrode surfaces. In: Bard AJ, Rubinstein I (eds) Electroanalytical chemistry, a series of advances, vol 20. Marcel Dekker, New York, pp 1–86
18. Grygar T, Marken F, Schröder U, Scholz F (2002) Collect Czech Chem Commun 67:163–208
19. Scholz F, Schröder U, Gulaboski R (2005) Electrochemistry of immobilized particles and droplets. Springer, Berlin
20. Doménech A, Alarcón J (2002) J Solid State Electrochem 6:443–450
21. Doménech A, Aucejo R, Alarcón J, Navarro P (2004) Electrochem Commun 6:719–723
22. Doménech A, Alarcón J (2002) Anal Chim Acta 452:11–22
23. Doménech A, Alarcón J (2007) Anal Chem 79:6742–6751
24. Doménech A, Moyá M, Doménech MT (2004) Anal Bioanal Chem 380:146–156
25. Doménech A, Torres FJ, Ruiz de Sola E, Alarcón J (2006) Eur J Inorg Chem :638–648
26. Zhang J, Lever ABP, Pietro WJ (1994) Inorg Chem 33:1392–1398
27. Keita B, Belhouari A, Nadjo L, Contant R (1995) J Electroanal Chem 381:243–250
28. Doherty AP, Stanley MA, Leech D, Vos JG (1996) Anal Chim Acta 319:111–120
29. Sunohara S, Nishimura K, Yahikozawa K, Ueno M, Enyo M, Takasu Y (1993) J Electroanal Chem 354:161–171
30. Chen S-M (1998) J Electroanal Chem 475:23–30
31. Gao Z, Zhang Y, Wang G (1998) Anal Sci 14:1053–1058
32. McCormac T, Fabré B, Bidan G (1997) J Electroanal Chem 427:155–159
33. Liu SQ, Shi Z, Dong SJ (1998) Electroanalysis 10:891–896
34. Ouani R, Rahmanifar M-S, Naderi P (2008) Electroanalysis 10:1092–1098
35. Migita Y, Yokohama H, Minami A, Mori T, Nojiri M, Suzuki S, Yamaguchi K (2009) Electroanalysis 21:2441–2446
36. Zheng J, Lu T, Cotton TM, Chumanov G (1999) J Phys Chem B 103:6567–6572
37. Ranjit KT, Viswanathan B (2003) J Photochem Photobiol A Chem 154:299–302
38. Sun C-C, Chou T-C (1998) Ind Eng Chem Res 37:4207–4214
39. Sun C-C, Chou T-C (2000) J Molec Catal A Chem 151:133–145

40. Mirceski V, Komorsky-Lovric S, Lovric M (2007) Square wave voltammetry, theory and applications. Springer, Berlin
41. Bard AJ, Fan R-FF, Kwak J, Lev O (1989) Anal Chem 61:132–138
42. Bard AJ, Mirkin MV (2003) Scanning electrochemical microscopy. Taylor & Francis, Boca Raton
43. Mehrotra S, Bandyophyay AK (2007) J Alloys Comp 436:56–60
44. Warmkessel JM, Lin S-H, Eyring L (1969) Inorg Chem 8:875–882
45. Olazcuaga R, Le Polles G, Kira E, Le Flem G, Maestro P (1987) J Solid State Chem 71:570–573
46. Ocaña M, Caballero A, Gonzalez-Elipe AR, Tartaj P, Serna CJ (1998) J Solid State Chem 139:412–415
47. Ocaña M, Caballero A, Gonzalez-Elipe AR, Tartaj P, Serna CJ, Merino RI (1999) J Eur Ceram Soc 19:641–648
48. Lyons MEG, Lyons CH, Michas A, Bartlett PN (1992) Analyst 117:1271–1280
49. Trasatti S (1994) Transition metal oxides: versatile materials for electrocatalysis. In: Lipkowski J, Ross PN (eds) The electrochemistry of novel materials. VCH, New York, pp 207–295
50. Dharuman V, Chandrasekara Pillai K (2006) J Solid State Electrochem 10:967–979
51. Bard AJ, Parsons R, Jordan J (1985) Standard potentials in aqueous solutions. IUPAC-Marcel Dekker, New York
52. Dharuman V (2006) Chandrasekara Pillai K. J Solid State Electrochem 12:967–979
53. Brainina KhZ, Galperin LG, Galperin AL (2010) J Solid State Electrochem 14:981–988
54. Grygar T (1997) J Solid State Electrochem 1:77–82
55. Grygar T (1998) J Solid State Electrochem 2:127–136
56. Falgairette C, Xia C, Li YD, Harbich W, Foti G, Comninellis C (2010) J Appl Electrochem 40:1901–1907
57. Peng J, Zhu Y, Wang D, Jin X, Chen GZ (2009) J Mater Chem 19:2803–2809
58. Morss LR (1976) Chem Rev 76:827–841
59. Scholz F, Hermes M (1999) Electrochem Commun 1:345–348 (see corrigendum in Scholz F, Hermes M (2000) Electrochem Commun 2:814)
60. Doménech A, Formentín P, García H, Sabater MJ (2000) Eur J Inorg Chem :1339–1344
61. Doménech A, Sánchez S, Doménech MT, Gimeno JV, Bosch F, Yusá DJ, Saurí MC (2002) Electroanalysis 14:685–696
62. Lovric M, Hermes M, Scholz F (1998) J Solid State Electrochem 2:401–404
63. Trasatti S (1984) Electrochim Acta 29:1503–1512
64. Singh RN, Madani M, Koenig J-F, Poillerat G, Gautier JL, Chartier P (1990) J Appl Electrochem 20:442–446
65. Balamurugan A, Chen S-M (2007) J Solid State Electrochem 11:1679–1687
66. Karnicka K, Ekhard K, Guschin DA, Stoica L, Kulesza PJ, Schuhmann W (2007) Electrochem Commun 9:1998–2002
67. Guadagnini L, Maljusch A, Chen X, Neugebauer S, Tonelli D, Schuhmann W (2009) Electrochim Acta 54:3753–3758
68. Xu W, Liu Ch, Xing W, Lu T (2007) Electrochem Commun 9:180–184